Eur. Phys. J. Plus (2019) **134**: 172
DOI 10.1140/epjp/i2019-12564-7

THE EUROPEAN
PHYSICAL JOURNAL PLUS

Regular Article

Physical aspects of irreversibility in radiative flow of viscous material with cubic autocatalysis chemical reaction

Tasawar Hayat[1,2], Sania Javed[1], M. Ijaz Khan[1,a], M. Imran Khan[3,b], and Ahmed Alsaedi[2]

[1] Department of Mathematics, Quaid-I-Azam University 45320, Islamabad 44000, Pakistan
[2] Nonlinear Analysis and Applied Mathematics (NAAM) Research Group, Department of Mathematics, Faculty of Science, King Abdulaziz University, Jeddah 21589, Saudi Arabia
[3] Heriot Watt University, Edinburgh Campus, Edinburgh EH14 4AS, UK

Received: 1 August 2018 / Revised: 10 December 2018
Published online: 26 April 2019

Abstract. Analysis of irreversibility in flow by a stretchable surface has gained much consideration in recent years. Entropy optimization properly computes the second law thermodynamic irreversibilities. Therefore, deterioration of entropy proficiency results in a more useful energy transport process. In this article, a physical aspect of irreversibility in radiative flow of viscous material with quartic autocatalysis chemical reaction is addressed. The flow is discussed between two stretchable rotating disks. Heat transfer occurring in this physical problem is modelled through thermal radiation, Joule heating and viscous dissipation. This is the first time the concept of homogeneous-heterogeneous reactions has been studied with entropy generation. The nonlinear flow expressions are made dimensionless. The obtained equations are then tackled through the homotopy concept. The analysis discloses that the radiation parameter and Eckert number play a vital role in the enhancement of temperature field. The tangential velocity decreases *versus* the magnetic parameter. The radial component of velocity boosts close to lower disks and it decreases near the upper disks *versus* the Reynolds number. The variations in the Nusselt number and skin friction are presented graphically with various emerging variables. It is noticed that entropy rate can be controlled by minimizing the impact of Brinkman and Reynolds numbers.

1 Introduction

The flow by a stretchable rotating disk has gained much consideration from investigators. It is because of its considerable applications in mechanical and industrial engineering processes like medical equipment, manufacturing, spin coating, centrifugal pumps, food processing technology, pumping of liquid metals *versus* high melting point, air cleaning machine, turbo-machinery, gas turbines, electric generating systems, etc. Keeping such motivation in mind, Karman [1] initially investigated the flow behavior by a rotating disk. Hayat *et al.* [2] explored irreversibility aspects in MHD radiative flow by a rotating disk via Joule heating and dissipations. Dissipative flow of second grade fluid is scrutinized by Hayat *et al.* [3]. Mustafa [4] analyzed MHD partial slip flow of nanomaterials by a rotating disk. Wu *et al.* [5] analyzed the two-phase air liquid flow through a rotating disk system with flow pattern maps. Hassan *et al.* [6] examined the mixed convective flow of ferroliquid with iron nanomaterials due to a rotating stretchable disk. Mehmood *et al.* [7] worked for MHD flow subject to a rotating disk. A comparative study of five different shape nanomaterials in rotating disk flow with velocity slip and Joule heating was discussed by Sumaira *et al.* [8]. Xun *et al.* [9] highlighted the heat transport in flow of Ostwald-de Waele liquid with index decreasing over a rotating disk. Lok *et al.* [10] considered axisymmetric stagnation point rotational flow by a permeable rotating disk. Some latest findings regarding this direction are listed in refs. [11–15].

The entropy optimization in recent years has been taken into consideration by many engineers and scientists to achieve the optimal design of thermal devices. In numerous heat transport mechanisms, a heat exchanger from higher to lower is the conventional heat transport tool. Thermal properties are improved through active and passive

[a] e-mail: mikhan@math.qau.edu.pk
[b] e-mail: mk42@hw.ac.uk (corresponding author)

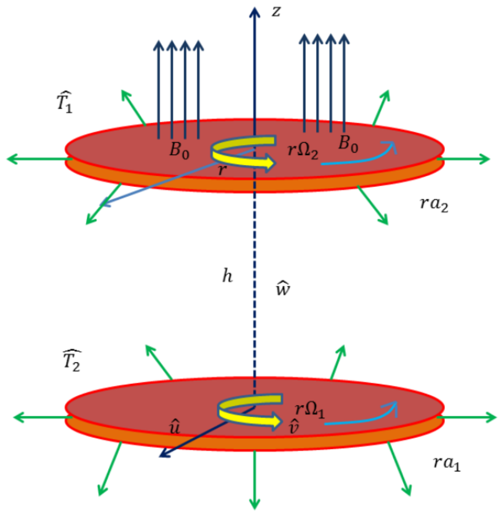

Fig. 1. Schematic flow diagram.

techniques. Numerous nanomaterials are utilized to enhance the heat transfer [16,17]. Ijaz *et al.* [18] have discussed irreversibility associated with flow and heat transport in Sisko nanoliquid by a rotating disk. Manay *et al.* [19] analyzed the nanomaterial flow in microchannel heat generation with entropy concept. Entropy generation associated with heat conduction in a fixed (adiabatic) cylinder was discussed by Tian and Wang [20]. Nanomaterial entropy optimization with helical twisted tapes was explored by Li *et al.* [21]. Kefayati *et al.* [22] studied diffusive double forced convective flow of Carreau liquid with entropy generation by a cold cylinder. Khan *et al.* [23] highlighted the entropy generation in tangent hyperbolic nanomaterial via nonlinear mixed convection and activation energy. Sadaf *et al.* [24] scrutinized the entropy generation in peristalsis flow with various nanomaterials shapes. Xie and Jian [25] investigated two-layer MHD electroosmotic flow with entropy generation via microparallel channels. Related investigations regarding entropy concept are listed in refs. [26–30].

Here entropy generation in radiative flow of viscous material between two rotating disks is addressed. The impacts of homogeneous-heterogeneous reactions are considered. The energy equation is modelled subject to dissipation, Joule heating and radiation. Through the implementation of the second law of thermodynamics the total entropy rate is calculated. The present flow expressions are made dimensionless by suitable transformations. The homotopy analysis method [31–45] is used to obtain the convergent series solutions. Nusselt numbers and skin friction coefficients at both upper and lower disks are discussed.

2 Mathematical description

2.1 Flow expression

Flow of viscous material in the presence of entropy generation and radiation is addressed. The flow is studied between two rotating disks. The lower disk (at $z=0$) is rotating with Ω_1 in axial direction while the upper disk (at $z=h$) rotates with Ω_2. Both disks are stretched respectively with stretching rates a_1 and a_2. The magnetic field is implemented in the z-direction. The schematic flow description is highlighted in fig. 1. The basic equations of the governing problem in vector form are

$$\boldsymbol{\nabla}\cdot\mathbf{V}=0, \tag{1}$$

$$(\mathbf{V}\cdot\boldsymbol{\nabla})\tilde{u}=-\frac{1}{\rho}\frac{\partial\tilde{p}}{\partial r}+\nu\boldsymbol{\nabla}^2\tilde{u}-\frac{\sigma}{\rho}B_0^2\tilde{u}, \tag{2}$$

$$(\mathbf{V}\cdot\boldsymbol{\nabla})\tilde{v}=\nu\boldsymbol{\nabla}^2\tilde{v}-\frac{\sigma}{\rho}B_0^2\tilde{v}, \tag{3}$$

$$(\mathbf{V}\cdot\boldsymbol{\nabla})\tilde{w}=-\frac{1}{\rho}\frac{\partial\tilde{p}}{\partial z}+\nu\boldsymbol{\nabla}^2\tilde{w}. \tag{4}$$

The flow equations are presented as [14]

$$\frac{\partial \tilde{u}}{\partial r} + \frac{\tilde{u}}{r} + \frac{\partial \tilde{w}}{\partial z} = 0, \tag{5}$$

$$\tilde{u}\frac{\partial \tilde{u}}{\partial r} + \tilde{w}\frac{\partial \tilde{u}}{\partial z} - \frac{\tilde{v}^2}{r} = -\frac{1}{\rho}\frac{\partial \tilde{p}}{\partial r} + \nu\left(\frac{\partial^2 \tilde{u}}{\partial r^2} + \frac{1}{r}\frac{\partial \tilde{u}}{\partial r} + \frac{\partial^2 \tilde{u}}{\partial z^2} - \frac{\tilde{u}}{r^2}\right) - \frac{\sigma}{\rho}B_0^2\tilde{u}, \tag{6}$$

$$\tilde{u}\frac{\partial \tilde{v}}{\partial r} + \tilde{w}\frac{\partial \tilde{v}}{\partial z} + \frac{\tilde{u}\tilde{v}}{r} = \nu\left(\frac{\partial^2 \tilde{v}}{\partial r^2} + \frac{1}{r}\frac{\partial \tilde{v}}{\partial r} + \frac{\partial^2 \tilde{v}}{\partial z^2} - \frac{\tilde{v}}{r^2}\right) - \frac{\sigma}{\rho}B_0^2\tilde{v}, \tag{7}$$

$$\tilde{w}\frac{\partial \tilde{w}}{\partial r} + \tilde{u}\frac{\partial \tilde{w}}{\partial r} = -\frac{1}{\rho}\frac{\partial \tilde{p}}{\partial z} + \nu\left(\frac{\partial^2 \tilde{w}}{\partial r^2} + \frac{1}{r}\frac{\partial \tilde{w}}{\partial r} + \frac{\partial^2 \tilde{w}}{\partial z^2}\right), \tag{8}$$

with the boundary conditions [39]

$$\begin{aligned} &\tilde{u} = ra_1, \quad \tilde{v} = r\Omega_1, \quad \tilde{w} = 0 \quad \text{at } z = 0,\\ &\tilde{u} = ra_2, \quad \tilde{v} = r\Omega_2, \quad \text{at } z = h. \end{aligned} \tag{9}$$

In the above expressions, the velocity components are denoted by $\tilde{u}$, $\tilde{v}$, $\tilde{w}$ and r, θ, z are the Cartesian coordinates, ρ denotes the density, $\tilde{p}$ represents the pressure, ν denotes the kinematic viscosity, σ represents the electrical conductivity, B_0 and h indicate the distance between two disks.

Considering the following transformations,

$$\hat{u} = r\Omega_1\hat{f}'(\xi), \qquad \tilde{v} = r\Omega_1\hat{g}(\xi), \qquad \tilde{w} = -2h\Omega_1\hat{f}(\xi), \qquad \tilde{p} = \rho_f\Omega_1\nu\left(\hat{P}(\xi) + \frac{1}{2}\frac{r^2}{h^2}\varepsilon\right), \tag{10}$$

the flow expressions take the following form:

$$\hat{f}''' + Re\left(2\hat{f}\hat{f}'' - \hat{f}'^2 + \hat{g}^2 - M\hat{f}'\right) - \varepsilon = 0, \tag{11}$$

$$\hat{g}'' + Re\left(2\hat{f}\hat{g}' - 2\hat{f}'\hat{g} - M\hat{g}\right) = 0, \tag{12}$$

$$\hat{P}' = -4Re\hat{f}\hat{f}' - 2\hat{f}'' \tag{13}$$

and the boundary conditions

$$\hat{f}(0) = 0, \qquad \hat{f}(1) = 0, \qquad \hat{f}'(0) = A_1, \qquad \hat{f}'(1) = A_2, \qquad \hat{g}(0) = 1, \qquad \hat{g}(1) = \Omega, \qquad \hat{P}(0) = 0, \tag{14}$$

where $Re(=\frac{\Omega_1 h^2}{\nu})$ highlights the Reynolds number, $M(=\frac{B_0^2\sigma}{\rho\Omega_1})$ denotes the magnetic parameter, $A_1(=\frac{a_1}{\Omega_1})$ and $A_2(=\frac{a_2}{\Omega_1})$ represents the ratio parameters and ε highlights the constant pressure.

Simplifying eq. (7) and omitting ε, one has

$$\hat{f}'''' + Re\left(2\hat{f}\hat{f}''' + 2\hat{g}\hat{g}' - M\hat{f}''\right) = 0. \tag{15}$$

From eq. (7), the pressure term is

$$\varepsilon = \hat{f}'''(0) - Re\left[(\hat{f}'(0))^2 - (\hat{g}(0))^2 + M\hat{f}'(0)\right]. \tag{16}$$

Integrating eq. (9) w.r.t ξ, one obtains

$$\hat{P} = -2\left[Re\hat{f}^2 + \left(\hat{f}' - \hat{f}'(0)\right)\right]. \tag{17}$$

2.2 Energy equation

Mathematically, the energy equation subject to dissipation, thermal radiation and Joule heating is expressed as

$$(\rho c_p)\left(\tilde{u}\frac{\partial \tilde{T}}{\partial r} + \tilde{w}\frac{\partial \tilde{T}}{\partial z}\right) = \left(k + \frac{16\sigma^\circ\tilde{T}_2^3}{3k^\circ}\right)\left(\frac{1}{r}\frac{\partial \tilde{T}}{\partial r} + \frac{\partial^2 \tilde{T}}{\partial r^2} + \frac{\partial^2 \tilde{T}}{\partial z^2}\right) + \sigma B_0^2(\tilde{u}^2 + \tilde{v}^2) + \mu\Phi, \tag{18}$$

where the mathematical form of (Φ) is defined as

$$\Phi = \left[2\left(\frac{\partial\tilde{u}}{\partial r}\right)^2 + 2\frac{\tilde{u}^2}{r^2} + 2\left(\frac{\partial\tilde{w}}{\partial z}\right)^2 + \left(\frac{\partial\tilde{v}}{\partial z}\right)^2 + \left(\frac{\partial\tilde{u}}{\partial z}\right)^2 + \left(r\frac{\partial}{\partial r}\left(\frac{\tilde{v}}{r}\right)\right)^2\right]. \tag{19}$$

From eqs. (14) and (15), we get the following expression:

$$\begin{aligned}(\rho c_p)\left(\tilde{u}\frac{\partial\tilde{T}}{\partial r} + \tilde{w}\frac{\partial\tilde{T}}{\partial z}\right) &= \left(k + \frac{16\sigma^\circ\tilde{T}_2^3}{3k^\circ}\right)\left(\frac{1}{r}\frac{\partial\tilde{T}}{\partial r} + \frac{\partial^2\tilde{T}}{\partial r^2} + \frac{\partial^2\tilde{T}}{\partial z^2}\right) + \sigma B_0^2(\tilde{u}^2 + \tilde{v}^2)\\ &+ \mu\left[2\left(\frac{\partial\tilde{u}}{\partial r}\right)^2 + 2\frac{\tilde{u}^2}{r^2} + 2\left(\frac{\partial\tilde{w}}{\partial z}\right)^2 + \left(\frac{\partial\tilde{v}}{\partial z}\right)^2 + \left(\frac{\partial\tilde{u}}{\partial z}\right)^2 + \left(r\frac{\partial}{\partial r}\left(\frac{\tilde{v}}{r}\right)\right)^2\right],\end{aligned} \tag{20}$$

with

$$\tilde{T} = \tilde{T}_1, \qquad \tilde{T} = \tilde{T}_2, \tag{21}$$

in which $\tilde{T}_1$ denotes the temperature at the lower disk, k° represents the mean absorption coefficient, c_p indicates the specific heat capacity, $\tilde{T}_2$ denotes the temperature atthe upper disk, k represents the thermal conductivity, μ presents the dynamic viscosity and σ° indicates the Stefan Boltzmann constant.

Considering the following transformations for energy equation,

$$\hat{\theta} = \frac{\tilde{T} - \tilde{T}_2}{\tilde{T}_1 - \tilde{T}_2}, \tag{22}$$

we have from energy equation

$$\frac{1}{\Pr}(1+R)\hat{\theta}'' + 2Re\hat{f}\hat{\theta}' + ReMEc(\hat{f}'^2 + \hat{g}^2) + 12EcA\hat{f}'^2 + Ec\hat{g}'^2 + Ec\hat{f}''^2 = 0, \tag{23}$$

$$\hat{\theta}(0) = 1, \qquad \hat{\theta}(1) = 0, \tag{24}$$

where $\Pr(=\frac{(\rho c_p)\nu}{k})$ represents the Prandtl number, $R(=\frac{16\sigma^\circ\tilde{T}_2^3}{3kk^\circ})$ denotes the radiation parameter, $Ec(=\frac{r^2\Omega_1^2}{c_p(\hat{T}_1-\hat{T}_2)})$ represents the Eckert number and $A(=\frac{h^2}{r^2})$.

2.3 Mass concentration via quartic chemical reaction

The mathematical form of the isothermal chemical reaction is defined as

$$A + 2B \to 3B, \quad \text{with reaction rate } C_R = k_c\hat{C}_1\hat{C}_2^2, \tag{25}$$

where species B has a higher concentration at the disk surface. The first-order isothermal heterogeneous reaction is of the form

$$A \to B \quad \text{with reaction rate } C_R = k_s\hat{C}_1, \tag{26}$$

in which A, B denotes the chemical species, k_c, k_s the reaction rates and $\hat{C}_1$ and $\hat{C}_2$ the concentrations. The concentration equation in terms of homogeneous-heterogeneous reactions is defined as

$$\tilde{u}\frac{\partial\tilde{C}_1}{\partial r} + \hat{w}\frac{\partial\tilde{C}_1}{\partial z} = D_{C_1}\left(\frac{\partial^2\tilde{C}_1}{\partial r^2} + \frac{1}{r}\frac{\partial\tilde{C}_1}{\partial r} + \frac{\partial^2\tilde{C}_1}{\partial z^2}\right) - k_c\tilde{C}_1\tilde{C}_2^2, \tag{27}$$

$$\hat{u}\frac{\partial\tilde{C}_2}{\partial r} + \hat{w}\frac{\partial\tilde{C}_2}{\partial z} = D_{C_2}\left(\frac{\partial^2\tilde{C}_2}{\partial r^2} + \frac{1}{r}\frac{\partial\tilde{C}_2}{\partial r} + \frac{\partial^2\tilde{C}_2}{\partial z^2}\right) + k_c\tilde{C}_1\tilde{C}_2^2, \tag{28}$$

with appropriate boundary conditions

$$\begin{aligned}D_{C_1}\frac{\partial\tilde{C}_1}{\partial z} = k_s\tilde{C}_1, \quad D_{C_2}\frac{\partial\tilde{C}_2}{\partial z} = -k_s\tilde{C}_1 \quad \text{at } z = 0,\\ \tilde{C}_1 \to \tilde{C}_\infty, \quad \tilde{C}_2 \to 0 \quad \text{at } z = h.\end{aligned} \tag{29}$$

Implementing the following transformations,

$$\hat{\varphi} = \frac{\tilde{C}_1}{\tilde{C}_\infty}, \qquad \hat{l} = \frac{\tilde{C}_2}{\tilde{C}_\infty}, \tag{30}$$

we obtain the following expressions:

$$\frac{1}{R^*}\left(\frac{1}{Sc}\right)\hat{\varphi}'' + 2\hat{f}\hat{\varphi}' - k_1\hat{\varphi}\hat{l}^2 = 0, \tag{31}$$

$$\frac{1}{R^*}\left(\frac{\delta}{Sc}\right)\hat{l}'' + 2\hat{f}\hat{l}' + k_1\hat{\varphi}\hat{l}^2 = 0, \tag{32}$$

with

$$\hat{\varphi}'(0) = k_2\hat{\varphi}(0), \qquad \hat{\varphi}(1) = 1, \qquad \delta\hat{l}'(0) = -k_2\hat{\varphi}(0), \qquad \hat{l}(1) = 0, \tag{33}$$

in which $Sc(=\frac{\nu}{D_{C_1}})$ indicates the Schmidt number, $k_1(=\frac{k_c\tilde{C}_\infty^2}{\Omega_1})$ denotes the homogeneous reaction parameter, $k_2(=\frac{k_s h}{D_{C_1}})$ represents the heterogeneous reaction parameter and $\delta(=\frac{D_{C_2}}{D_{C_1}})$ denotes the diffusion ratio parameter. For comparable chemical species A and B, we put $D_{C_1} = D_{C_2}$, *i.e.*, $\delta = 1$. Therefore we have the following relation:

$$\hat{\varphi}(\eta) + \hat{l}(\eta) = 1. \tag{34}$$

From eqs. (27) and (28) we have

$$\frac{1}{R^*}\left(\frac{1}{Sc}\right)\hat{\varphi}'' + 2\hat{f}\hat{\varphi}' - k_1\hat{\varphi}(1-\hat{\varphi})^2 = 0, \tag{35}$$

$$\hat{\varphi}'(0) = k_2\hat{\varphi}(0), \qquad \hat{\varphi}(1) = 1. \tag{36}$$

3 Physical quantities

3.1 Skin friction coefficients

The shear stresses, *i.e.*, (τ_{zr}) and $(\tau_{z\theta})$ at the lower disk are expressed as

$$\tau_{zr} = \mu\frac{\partial\tilde{u}}{\partial z} = \frac{\mu r\Omega_1\hat{f}''(\xi)}{h}, \qquad \tau_{z\theta} = \mu\frac{\partial\tilde{v}}{\partial z} = \frac{\mu r\Omega_1\hat{g}'(\xi)}{h}. \tag{37}$$

The total shear stress τ_w is

$$\tau_w = \sqrt{\tau_{zr}^2 + \tau_{z\theta}^2}. \tag{38}$$

Finally,

$$\begin{aligned} C_{f1} &= \frac{\tau_w|_{z=0}}{\rho(r\Omega_1)^2} = \frac{1}{R_r}\left[\left(\hat{f}''(0)\right)^2 + \left(\hat{g}'(0)\right)^2\right]^{1/2}, \\ C_{f2} &= \frac{\tau_w|_{z=h}}{\rho(r\Omega_1)^2} = \frac{1}{R_r}\left[\left(\hat{f}''(1)\right)^2 + \left(\hat{g}'(1)\right)^2\right]^{1/2}. \end{aligned} \tag{39}$$

3.2 Nusselt number

At upper and lower disks, it is mathematically defined as

$$Nu_{x1} = \left.\frac{hq_w}{k(\tilde{T}_1 - \tilde{T}_2)}\right|_{z=0}, \qquad Nu_{x2} = \left.\frac{hq_w}{k(\tilde{T}_1 - \tilde{T}_2)}\right|_{z=h}, \tag{40}$$

where q_w for lower and upper disks are

$$q_w|_{z=0} = -k\frac{\partial \tilde{T}}{\partial z} + q_r|_{z=0} = -\frac{(\tilde{T}_1 - \tilde{T}_2)}{h}\left(k + \frac{16\sigma^\circ \tilde{T}_2^3}{3k^\circ}\right)\tilde{\theta}'(0),$$
$$q_w|_{z=h} = -k\frac{\partial \tilde{T}}{\partial z} + q_r|_{z=h} = -\frac{(\hat{T}_1 - \hat{T}_2)}{h}\left(k + \frac{16\sigma^\circ \tilde{T}_2^3}{3k^\circ}\right)\tilde{\theta}'(1). \quad (41)$$

Finally,

$$Nu_{x1} = -(1+R)\tilde{\theta}'(0), \qquad Nu_{x2} = -(1+R)\tilde{\theta}'(1). \quad (42)$$

In the above expressions C_{f1} denotes the skin friction at the lower disk, C_{f2} represents the skin friction at the upper disk, τ_{zr} highlights the shear stress in the radial direction, $\tau_{z\theta}$ denotes the shear stress in the tangential direction, τ_w represents the total shear stress, Nu_{x1} indicates the Nusselt at the lower disk, Nu_{x2} highlights the Nusselt number at the upper disk and $R_r(=\frac{r\Omega_1 h}{\nu})$ denotes the local Reynolds number.

4 Entropy equation

We have

$$S_G = \frac{k}{\tilde{T}^2}\left[1 + \frac{16\sigma^* \tilde{T}_2^3}{3kk^*}\right]\left[\left(\frac{\partial \tilde{T}}{\partial z}\right)^2 + \left(\frac{\partial \tilde{T}}{\partial r}\right)^2\right] + \frac{\sigma}{T}B_0^2\left(\tilde{u}^2 + \tilde{v}^2\right)$$
$$+ \frac{\mu}{\tilde{T}}\left[2\left(\frac{\partial \tilde{u}}{\partial r}\right)^2 + 2\frac{\tilde{u}^2}{r^2} + 2\left(\frac{\partial \tilde{w}}{\partial z}\right)^2 + \left(\frac{\partial \tilde{v}}{\partial z}\right)^2 + \left(\frac{\partial \tilde{u}}{\partial z}\right)^2 + \left(r\frac{\partial}{\partial r}\left(\frac{\tilde{v}}{r}\right)\right)^2\right]$$
$$+ \frac{R^* D_{C_1}}{\tilde{C}_1}\left[\left(\frac{\partial \tilde{C}_1}{\partial z}\right)^2 + \left(\frac{\partial \tilde{C}_1}{\partial r}\right)^2\right] + \frac{R^* D_{C_1}}{\tilde{T}}\left(\frac{\partial \tilde{C}_1}{\partial r}\frac{\partial \tilde{T}}{\partial r} + \frac{\partial \tilde{C}_1}{\partial z}\frac{\partial \tilde{T}}{\partial z}\right)$$
$$+ \frac{R^* D_{C_2}}{\tilde{C}_2}\left[\left(\frac{\partial \tilde{C}_2}{\partial r}\right)^2 + \left(\frac{\partial \tilde{C}_2}{\partial z}\right)^2\right] + \frac{R^* D_{C_2}}{\tilde{T}}\left(\frac{\partial \tilde{C}_2}{\partial r}\frac{\partial \tilde{T}}{\partial r} + \frac{\partial \tilde{C}_2}{\partial z}\frac{\partial \tilde{T}}{\partial z}\right). \quad (43)$$

The dimensionless form is

$$N_G = \frac{(1+R)\alpha_1 \hat{\theta}'^2}{(\hat{\theta}(\theta_w - 1) + 1)^2} + \frac{Br A}{(\hat{\theta}(\theta_w - 1) + 1)}\left(12\hat{f}'^2 + A\left(\hat{g}'^2 + \hat{f}''^2\right)\right) + \frac{M Br\,\mathrm{Re}}{(\hat{\theta}(\theta_w - 1) + 1)}\left(\hat{f}'^2 + \hat{g}^2\right)$$
$$+ \frac{\hat{\varphi}'^2}{\alpha_1}\left(\frac{L_1}{\hat{\varphi}} + \frac{L_2}{(1-\hat{\varphi})}\right) + \frac{\hat{\theta}'\hat{\varphi}'}{(\hat{\theta}(\theta_w - 1) + 1)}(L_1 - L_2), \quad (44)$$

where $Br(=\frac{\mu\gamma^2\Omega_1^2}{k\Delta T})$ represents the Brinkman number, $\alpha_1(=\frac{\Delta T}{T_2})$ denotes the temperature difference parameter, $A(=\frac{h^2}{r^2})$ represents the dimensionless parameter, $N_G(=\frac{S_G T_2 h^2}{k\Delta T})$ highlights the entropy generation rate, $L_1(=\frac{R^* D_{C_1} C_\infty}{k})$ denotes the diffusion variable with respect to the homogeneous reaction and $L_2(=\frac{R^* D_{C_2} C_\infty}{k})$ indicates the diffusion variable with respect to the heterogeneous reaction.

The Bejan number is expressed as

$$Be = \frac{Entropy\ generation\ due\ to\ heat\ and\ mass\ transfer}{Total\ entropy\ generation}.$$

5 Methodology

5.1 Zero-th–order problems

Initial approximations and auxiliary linear operators are

$$\begin{aligned}
\hat{f}_0(\xi) &= A_1\xi - 2A_1\xi^2 - A_2\xi^2 + A_1\xi^3 + A_2\xi^3,\\
\hat{g}_0(\xi) &= 1 + (\Omega - 1)\xi,\\
\hat{\theta}_0(\xi) &= 1 - \xi,\\
\hat{\varphi}_0(\xi) &= \frac{1 + k_2\xi}{1 + k_2}\,,
\end{aligned} \tag{45}$$

$$\begin{aligned}
\mathbf{L}_{\hat{f}} &= \hat{f}'''',\\
\mathbf{L}_{\hat{g}} &= \hat{g}'',\\
\mathbf{L}_{\hat{\theta}} &= \hat{\theta}'',\\
\mathbf{L}_{\hat{\varphi}} &= \hat{\varphi}'',
\end{aligned} \tag{46}$$

with

$$\begin{aligned}
&\mathbf{L}_{\hat{f}}\left[\alpha_1^* + \alpha_2^*\xi + \alpha_3^*\xi^2 + \alpha_4^*\xi^3\right] = 0,\\
&\mathbf{L}_{\hat{g}}[\alpha_5^* + \alpha_6^*\xi] = 0,\\
&\mathbf{L}_{\hat{\theta}}\left[\alpha_7^* + \alpha_8^*\xi\right] = 0,\\
&\mathbf{L}_{\hat{\varphi}}\left[\alpha_9^* + \alpha_{10}^*\xi\right] = 0,
\end{aligned} \tag{47}$$

where α_i^* $(i = 1, 2, 3, \ldots, 10)$ are constants.

Let $q^* \in [0, 1]$ be the embedding variable and $h_{\hat{f}}$, $h_{\hat{g}}$, $h_{\hat{\theta}}$ and $h_{\hat{\varphi}}$ the non-zero auxiliary variables then zero-th–order deformations are

$$(1 - q^*)\mathbf{L}_{\hat{f}}\left[\hat{F}(\xi; q^*) - \hat{f}_0(\xi)\right] = q^* h_{\hat{f}}\mathbf{N}_{\hat{f}}\left[\hat{F}(\xi; q^*), \hat{G}(\xi; q^*)\right], \tag{48}$$

$$(1 - q^*)\mathbf{L}_{\hat{g}}\left[\hat{G}(\xi; q^*) - \hat{g}_0(\xi)\right] = q^* h_{\hat{g}}\mathbf{N}_{\hat{g}}\left[\hat{G}(\xi; q^*), \hat{F}(\xi; q^*)\right], \tag{49}$$

$$(1 - q^*)\mathbf{L}_{\hat{\theta}}\left[\hat{\vartheta}(\xi; q^*) - \hat{\theta}_0(\xi)\right] = q^* h_{\hat{\theta}}\mathbf{N}_{\hat{\theta}}\left[\hat{\vartheta}(\xi; q^*), \hat{F}(\xi; q^*), \hat{G}(\xi; q^*)\right], \tag{50}$$

$$(1 - q^*)\mathbf{L}_{\hat{\varphi}}\left[\hat{\Phi}(\xi; q^*) - \hat{\varphi}_0(\xi)\right] = q^* h_{\hat{\varphi}}\mathbf{N}_{\hat{\varphi}}\left[\hat{\Phi}(\xi; q^*), \hat{F}(\xi; q^*)\right], \tag{51}$$

with the conditions

$$\hat{F}(0; q^*) = 0, \qquad \hat{F}(1; q^*) = 0, \qquad \hat{F}^{'}(0; q^*) = A_1, \qquad \hat{F}'(1; q^*) = A_2, \tag{52}$$

$$\hat{G}(0; q^*) = 1, \qquad \hat{G}(1; q^*) = \Omega, \tag{53}$$

$$\hat{\vartheta}(0; q^*) = 1, \qquad \hat{\vartheta}(1; q^*) = 0, \tag{54}$$

$$\hat{\Phi}'(0; q^*) - k_2\hat{\Phi}(0; q^*) = 0, \qquad \hat{\Phi}(1; q^*) = 1. \tag{55}$$

Nonlinear operator $\mathbf{N}_{\hat{f}}$, $\mathbf{N}_{\hat{g}}$, $\mathbf{N}_{\hat{\theta}}$ and $\mathbf{N}_{\hat{\varphi}}$ are

$$\mathbf{N}_{\hat{f}}\left[\hat{F}(\xi; q^*), \hat{G}(\xi; q^*), \hat{\theta}(\xi; q^*), \hat{\varphi}(\xi; q^*)\right] = \frac{\partial^4 \hat{F}(\xi; q^*)}{\partial \xi^4} + R\left[2\hat{G}(\xi; q^*)\frac{\partial \hat{g}(\xi; q^*)}{\partial \xi} + 2\hat{F}(\xi; q^*)\frac{\partial^3 \hat{F}(\xi; q^*)}{\partial \xi^3} - M\frac{\partial^2 \hat{F}(\xi; q^*)}{\partial \xi^2}\right] \tag{56}$$

$$\mathbf{N}_{\hat{g}}\left[\hat{G}(\xi; q^*), \hat{F}(\xi; q^*)\right] = \frac{\partial^2 \tilde{G}(\xi; q^*)}{\partial \xi^2} + R\left[2\hat{F}(\xi; q^*)\frac{\partial \hat{G}(\xi; q^*)}{\partial \xi} - 2\frac{\partial \hat{F}(\xi; q^*)}{\partial \xi}\tilde{G}(\xi; q^*) - M\tilde{G}(\xi; q^*)\right] \tag{57}$$

$$\mathbf{N}_{\hat{\theta}}\left[\hat{\vartheta}(\eta;q^*),\hat{F}(\eta;q^*),\hat{G}(\xi;q^*)\right]=\frac{1}{\mathrm{Pr}}(1+R)\frac{\partial^2\hat{\vartheta}(\xi;q^*)}{\partial\xi^2}+2R\hat{F}(\xi;q^*)\frac{\partial\hat{\vartheta}(\xi;q^*)}{\partial\xi}$$
$$+MREc\left(\left(\frac{\partial\hat{F}(\xi;q^*)}{\partial\xi}\right)^2+\hat{G}^2(\xi;q^*)\right)+12EcA\left(\frac{\partial\hat{F}(\xi;q^*)}{\partial\xi}\right)^2+Ec\left(\frac{\partial\hat{G}(\xi;q^*)}{\partial\xi}\right)^2+Ec\left(\frac{\partial^2\hat{F}(\xi;q^*)}{\partial\xi^2}\right)^2, \quad (58)$$

$$\mathbf{N}_{\hat{\varphi}}\left[\hat{\Phi}(\xi;q^*),\hat{F}(\xi;q^*)\right]=\frac{1}{R}\frac{1}{Sc}\frac{\partial^2\hat{\Phi}(\xi;q^*)}{\partial\xi^2}+2\hat{F}(\xi;q^*)\frac{\partial\hat{\Phi}(\xi;q^*)}{\partial\xi}-k_1\hat{\Phi}(\xi;q^*)(1-\hat{\Phi}(\xi;q^*))^2. \quad (59)$$

5.2 m-th–order problems

We have

$$\mathbf{L}_{\tilde{f}}\left[\hat{f}_m(\xi)-\chi_m\hat{f}_{m-1}(\xi)\right]=h_{\hat{f}}\mathbf{R}_{\hat{f},m}(\xi), \quad (60)$$
$$\mathbf{L}_{\hat{g}}\left[\hat{g}_m(\xi)-\chi_m\hat{g}_{m-1}(\xi)\right]=h_{\hat{g}}\mathbf{R}_{\hat{g},m}(\xi), \quad (61)$$
$$\mathbf{L}_{\hat{\theta}}\left[\hat{\theta}_m(\xi)-\chi_m\hat{\theta}_{m-1}(\xi)\right]=h_{\hat{\theta}}\mathbf{R}_{\hat{\theta},m}(\xi), \quad (62)$$
$$\mathbf{L}_{\hat{\varphi}}\left[\hat{\varphi}_m(\xi)-\chi_m\hat{\varphi}_{m-1}(\xi)\right]=h_{\hat{\varphi}}\mathbf{R}_{\hat{\varphi},m}(\xi), \quad (63)$$
$$\chi_m=\begin{cases}0, & m\le 1,\\ 1, & m>1.\end{cases} \quad (64)$$
$$\hat{f}_m(0)=\frac{\partial\hat{f}_m(0)}{\partial\xi}=\frac{\partial\hat{f}_m(1)}{\partial\xi}=\hat{f}_m(1)=0,$$
$$\hat{g}_m(0)=\hat{g}_m(1)=\hat{\theta}_m(0)=\hat{\theta}_m(1)=0,$$
$$\hat{\varphi}'_m(0)-k_2\hat{\varphi}_m(0)=\hat{\varphi}_m(1)=0, \quad (65)$$
$$\mathbf{R}_{\hat{f},m}(\xi)=\hat{f}^{iv}_{m-1}+R\left(2\sum_{k=0}^{m-1}\left(\hat{f}'''_{m-1-k}\hat{f}_k+\hat{g}_{m-1-k}\hat{g}'_k\right)-M\hat{f}''_{m-1}\right), \quad (66)$$
$$\mathbf{R}_{\tilde{g},m}(\xi)=\tilde{g}''_{m-1}+R\left(2\sum_{k=0}^{m-1}\left(\hat{f}_{m-1-k}\hat{g}'_k-\hat{f}'_{m-1-k}\hat{g}_k\right)-M\hat{g}_{m-1}\right), \quad (67)$$
$$\mathbf{R}_{\tilde{\theta},m}(\eta)=\frac{1}{\mathrm{Pr}}(1+R)\hat{\theta}''_{m-1}+2R\sum_{k=0}^{m-1}\tilde{f}_{m-1-k}\tilde{\theta}'_k+MREc\left(\sum_{k=0}^{m-1}\tilde{f}'_{m-1-k}\tilde{f}'_k+\sum_{k=0}^{m-1}\tilde{g}_{m-1-k}\tilde{g}_k\right)$$
$$+12EcA\sum_{k=0}^{m-1}\tilde{f}'_{m-1-k}\tilde{f}'_k+Ec\sum_{k=0}^{m-1}\tilde{g}'_{m-1-k}\tilde{g}'_k+Ec\sum_{k=0}^{m-1}\tilde{f}''_{m-1-k}\tilde{f}''_k, \quad (68)$$
$$\mathbf{R}_{\tilde{\varphi},m}(\eta)=\frac{1}{R}\frac{1}{Sc}\hat{\varphi}''_{m-1}+\sum_{k=0}^{m-1}\left(2\tilde{f}_{m-1-k}\hat{\varphi}'_k+2k_1\hat{g}_{m-1-k}\hat{g}_k-k_1\hat{g}_{m-1-k}\sum_{l=0}^{k}\hat{g}_{k-l}\hat{g}_l\right)-k_1\hat{\varphi}_{m-1}. \quad (69)$$

The general solutions $(\hat{f}_m,\hat{g}_m,\hat{\theta}_m,\hat{\varphi}_m)$ through special solutions $(\hat{f}^*_m,\hat{g}^*_m,\hat{\theta}^*_m,\hat{\varphi}^*_m)$ are

$$\hat{f}_m(\xi)=\hat{f}^*_m(\xi)+\alpha^*_1+\alpha^*_2\xi+\alpha^*_3\xi^2+\alpha^*_4\xi^3, \quad (70)$$
$$\hat{g}_m(\xi)=\hat{g}^*_m(\xi)+\alpha^*_5+\alpha^*_6\xi, \quad (71)$$
$$\hat{\theta}_m(\xi)=\hat{\theta}^*_m(\xi)+\alpha^*_7+\alpha^*_8\xi, \quad (72)$$
$$\hat{\varphi}_m(\xi)=\hat{\varphi}^*_m(\xi)+\alpha^*_9+\alpha^*_{10}\xi. \quad (73)$$

6 Convergence analysis

In the homotopy analysis technique, the convergence control parameters have an essential role on convergence and approximation rate for series solutions. For suitable values of these parameters, the $\hbar$-curves are sketched at 13-th–order of approximations in fig. 2. The exact ranges for momentum, energy and concentration equations are $-2.2\le h_{\tilde{f}}\le 0.8$,

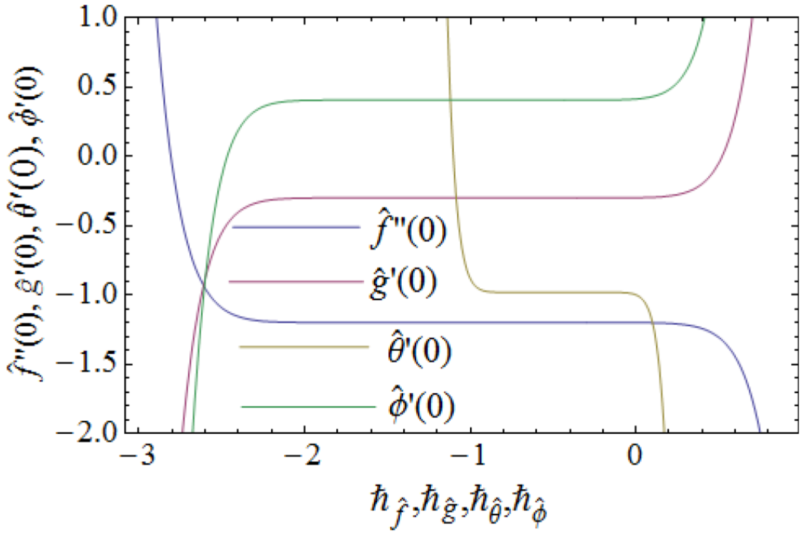

Fig. 2. h-curves for $\hat{f}''(0)$, $\hat{g}'(0)$, $\hat{\theta}'(0)$, $\widehat{\phi}'(0)$.

Table 1. Series solutions when $\Pr = 0.7$, $Re = 0.01$, $M = 0.4$, $A_1 = 0.1$, $A_2 = 0.4$, $\Omega = 1.0$, $R = 0.5$, $Ec = 0.1$, $Sc = 1.0$, $A = 1$, $k_1 = 0.4$ and $k_2 = 0.7$.

Order of approximations	$-\hat{f}''(0)$	$-\hat{g}'(0)$	$-\hat{\theta}'(0)$	$\hat{\phi}'(0)$
1	1.199445	0.3015600	0.9886505	0.4027557
3	1.199446	0.3013105	0.9831518	0.4038577
7	1.199446	0.3013001	0.9823611	0.4038813
8	1.199446	0.3013000	0.9823526	0.4038813
13	1.199446	0.3013000	0.9823480	0.4038813
20	1.199446	0.3013000	0.9823480	0.4038813
30	1.199446	0.3013000	0.9823480	0.4038813
40	1.199446	0.3013000	0.9823480	0.4038813

$-2.1 \leq h_{\tilde{g}} \leq 0.85$, $0.9 \leq h_{\tilde{\theta}} \leq 0.1$ and $-2.0 \leq h_{\tilde{\varphi}} \leq 0.1$. Table 1 is plotted for the convergence series solutions when $\Pr = 0.7$, $Re = 0.01$, $M = 0.4$, $A_1 = 0.1$, $A_2 = 0.4$, $\Omega = 1.0$, $R = 0.5$, $Ec = 0.1$, $Sc = 1.0$, $A = 1$, $k_1 = 0.4$ and $k_2 = 0.7$. It is noticed that the 3rd, 8th, 13th and 7th orders of approximations are sufficient for the convergence of $\hat{f}''(0)$, $\hat{g}'(0)$, $\hat{\theta}'(0)$ and $\hat{\varphi}'(0)$.

7 Discussion

A mathematical model is presented for the flow of viscous fluid subject to thermal radiation and dissipation between two rotating stretchable disks. The homotopy analysis method is implemented for the development of series solutions. In this portion, the effects of the different pertinent variables are discussed through plots. Table 1 is plotted for the convergent series solutions. Table 2 highlights the numerical results for skin friction coefficients in radial and tangential directions. From table 2 it is noted that higher values of magnetic parameter reduces the magnitude of (C_{f1}) at the lower disk while the magnitude of (C_{f2}) increases at the upper disk. Furthermore, the magnitude of (C_{f1}) and (C_{f2}) monotonically decreases *versus* higher values of the Reynolds number and (A_1). It is also noted that these two quantities have a reverse response at the upper disk. The impacts of the radiation parameter, Eckert number and Prandtl number on Nusselt numbers (Nu_{x1}, Nu_{x2}) at lower and upper disks are highlighted in table 3. Clearly, the transfer rate decreases at the lower disk when $(\Pr)$ and (Ec) are increased and increases *versus* larger (R). Physically for a larger Eckert number, the kinetic energy of the system increases, due to which temperature increases and thus the heat transfer rate decreases. Furthermore, the heat transfer rate increases at the upper disk for $(\Pr)$, (R) and (Ec).

Table 2. Numerical outcomes for C_{f1} and C_{f2} when M, A_1 and R.

M	Re	A_1	C_{f1}	C_{f2}
0.4	0.01	0.1	1.236710	1.825318
0.5			1.236819	1.825302
0.6			1.236929	1.825286
0.4	0.1		1.234769	1.829793
	0.2		1.232733	1.834905
	0.3		1.230825	1.840160
	0.01	0.2	1.627713	2.022884
		0.3	2.022300	2.220863

Table 3. Numerical outcomes for Nu_{x1} and Nu_{x2} when Pr, R and Ec.

Pr	R	Ec	Nu_{x1}	Nu_{x2}
0.7	0.5	0.1	1.473522	1.555976
0.8			1.469740	1.563973
0.9			1.465957	1.571970
0.7	0.6		1.573522	1.655976
	0.7		1.673522	1.755976
	0.8		1.773522	1.855976
	0.5	0.2	1.447161	1.611720
		0.3	1.420799	1.667463

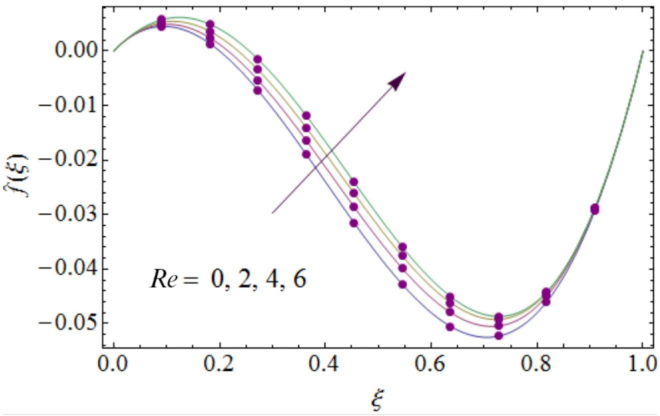

Fig. 3. $\hat{f}(\xi)$ against Re.

7.1 Velocity components: Radial ($\hat{\mathbf{f}}'(\xi)$), tangential ($\hat{\mathbf{g}}(\xi)$), axial ($\hat{\mathbf{f}}(\xi)$) velocities

Figures 3–5 are plotted for the impact of (Re) on radial ($\hat{f}'(\xi)$), tangential ($\hat{g}(\xi)$), axial ($\hat{f}(\xi)$) velocity components. In fig. 3, it is noted that the magnitude of ($\hat{f}(\xi)$) decreases when (Re) is enhanced, *i.e.* ($Re = 0, 2, 4, 6$). Physically the Reynolds number has a direct relation with inertial forces, therefore axial velocity is decreased. Dual behavior is noticed for ($\hat{f}'(\xi)$) *versus* larger (Re). Initially radial velocity increases closed to the lower disk and then it boosts slowly when the Reynolds number takes the maximum value. Physically inertial forces enhance which directly affect the velocity field. That is why velocity at the upper disk is higher than at the lower disk (fig. 4). As expected ($\hat{g}(\xi)$) decreases *versus* larger (Re) (fig. 5). Figure 6 describes the salient attributes of the magnetic parameter on tangential velocity. Physically magnetic parameter is the ratio of electromagnetic to viscous forces. Therefore, enhancement in the magnetic parameter creates the Lorentz force which causes flow to run in the opposite direction. Figures 7 and 8 report ($\hat{f}'(\xi)$) and ($\hat{f}(\xi)$) *versus* A_1. As expected, the axial component of velocity is enhanced for larger A_1. Physically stretching rate increases for higher A_1 (fig. 7). Dual effect of radial velocity is observed *versus* A_1.

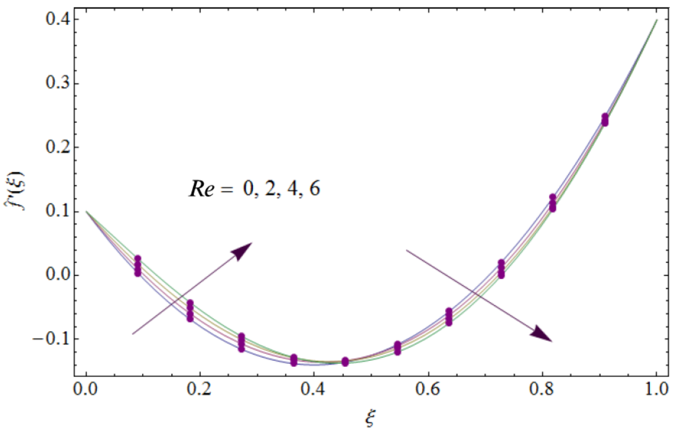

Fig. 4. $\hat{f}'(\xi)$ against Re.

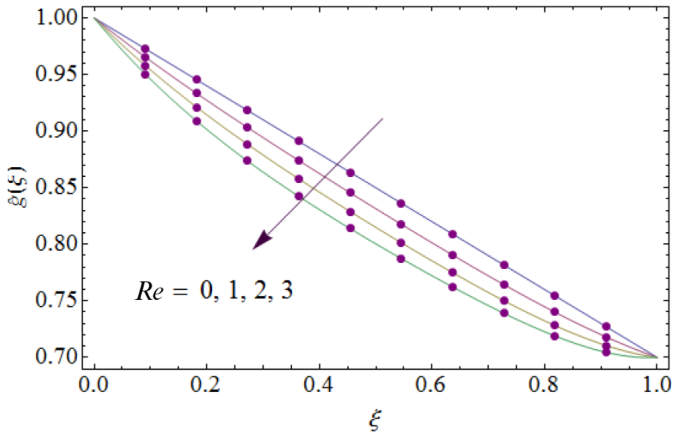

Fig. 5. $\hat{g}(\xi)$ against Re.

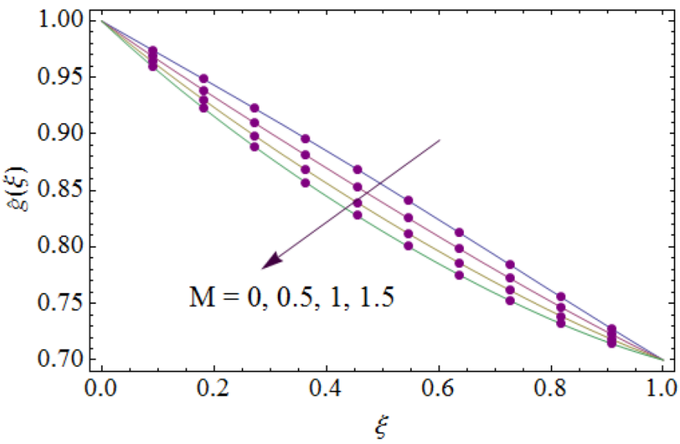

Fig. 6. $\hat{g}(\xi)$ against M.

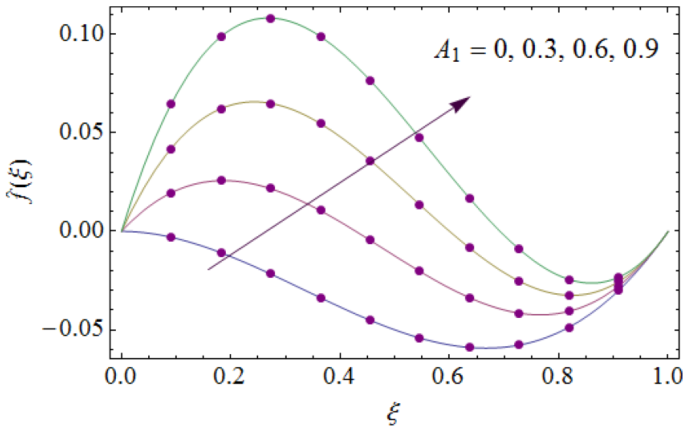

Fig. 7. $\hat{f}(\xi)$ against A_1.

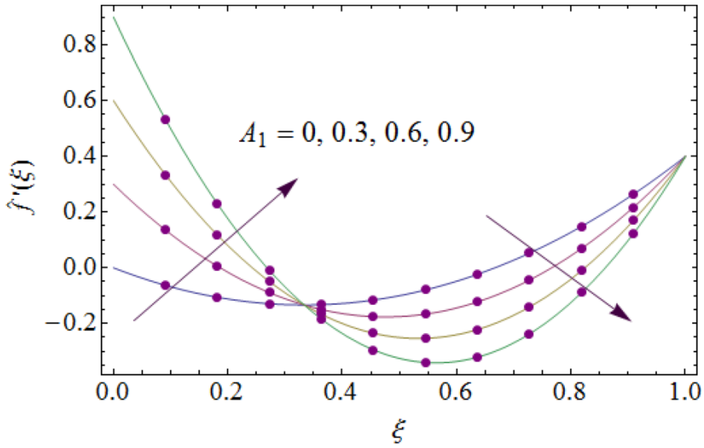

Fig. 8. $\hat{f}'(\xi)$ against A_1.

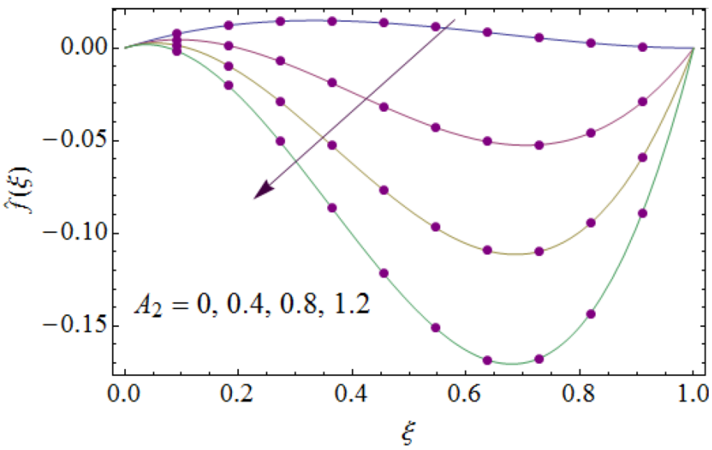

Fig. 9. $\hat{f}(\xi)$ against A_2.

Initially velocity increases closed to the lower disk and then it diminishes when A_1 reaches to the maximum value, *i.e.* $A_1 = 0.9$. The outcome of A_2 on axial velocity is displayed in fig. 9. It is shown that the magnitude of axial velocity decreases at both upper and lower disk for A_2. Figure 10 depicts the behavior of A_2 on $(\hat{f}'(\xi))$. The magnitude of $(\hat{f}'(\xi))$ decreases at the lower disk and it boosts at the upper disk through higher A_2. Note that the stretching rate is more at the upper disk than at the lower disk surface. Therefore, radial velocity enhances at the upper disk. Tangential velocity in fig. 11 rises *versus* rotation Ω.

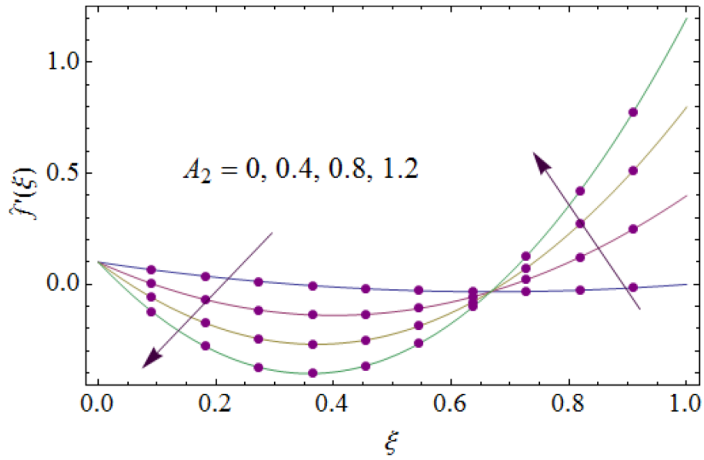

Fig. 10. $\hat{f}'(\xi)$ against A_2.

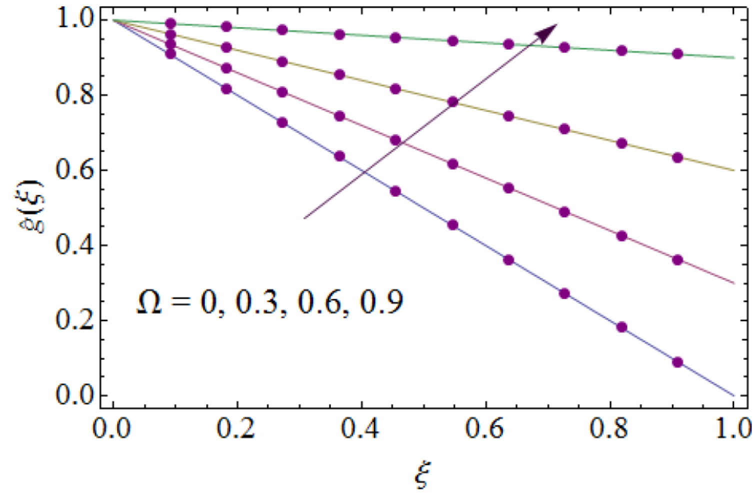

Fig. 11. $\hat{g}(\xi)$ against Ω.

7.2 Temperature field

In this subsection, figs. 12–15 show the graphical results for different variables like Pr, R, Ec and M on $(\hat{\theta}(\xi))$. Figure 12 delineates the impact of Pr on $(\hat{\theta}(\xi))$. It is examined that temperature decreases through higher Pr. The thermal layer thickness also diminishes slowly for higher Pr, *i.e.* $\mathrm{Pr} = 0.50, 0.55, 0.60, 1.0$. Physically larger Pr is responsible for thermal diffusivity which declines the temperature of liquid. Figure 13 detects the characteristics of radiation on $(\hat{\theta}(\xi))$. It is analyzed that temperature and layer thickness increase through higher R. A larger radiation parameter produces more heat in the working liquid through the radiation process which consequently boosts the thermal field. The curves of $(\hat{\theta}(\xi))$ *versus* (Ec) are highlighted in fig. 14. Physically, the ratio of kinetic energy to enthalpy or dynamic temperature to the temperature is called the Eckert number. Larger Ec boosts the kinetic energy of working fluid particles which results in the augmentation of the thermal field. Variation in the magnetic parameter on $(\hat{\theta}(\xi))$ is shown in fig. 15. Physically the magnetic parameter depends on the Lorentz force which is the resistive force to the liquid flow. It rises the kinetic energy on inside molecules or atoms. That is why temperature boosts.

7.3 Concentration

In this subsection, we established the graphical results for flow variables, *i.e.*, homogeneous reaction variable (k_1), Schmidt number (Sc) and heterogeneous variable (k_2) on $(\varphi(\xi))$. Figure 16 depicts the effect of (k_1) on $(\varphi(\xi))$. As expected, concentration decreases *versus* (k_1). Physically the reactants are consumed through larger (k_1) during the homogeneous reaction. Figure 17 has been plotted to detect the physical behavior of the heterogeneous reaction variable on $(\varphi(\xi))$. It is examined that the concentration of liquid particles on the disk surface decreases which directly affects

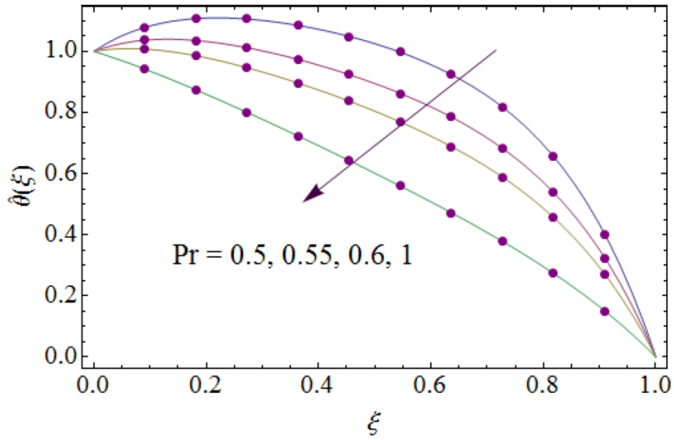

Fig. 12. $\widehat{\theta}(\xi)$ against Pr.

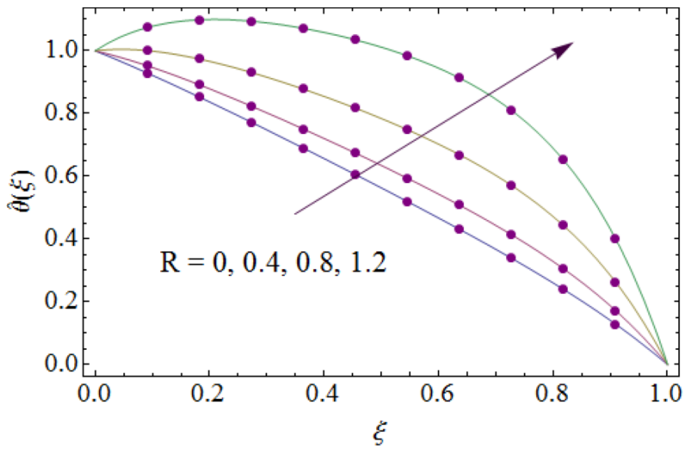

Fig. 13. $\widehat{\theta}(\xi)$ against R.

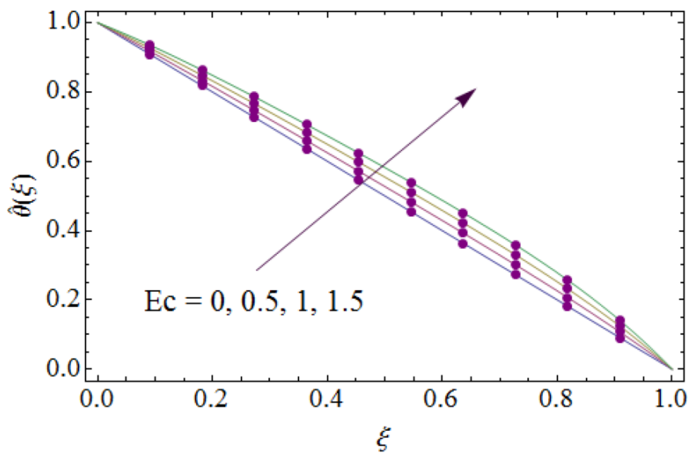

Fig. 14. $\widehat{\theta}(\xi)$ against Ec.

the concentration field. Figure 18 explores the physical explanation regarding the Schmidt number on $(\varphi(\xi))$. Since the ratio of momentum to mass diffusivities is known as the Schmidt number. Therefore momentum diffusivity intensifies through higher (Sc), which in turn increases $(\varphi(\xi))$.

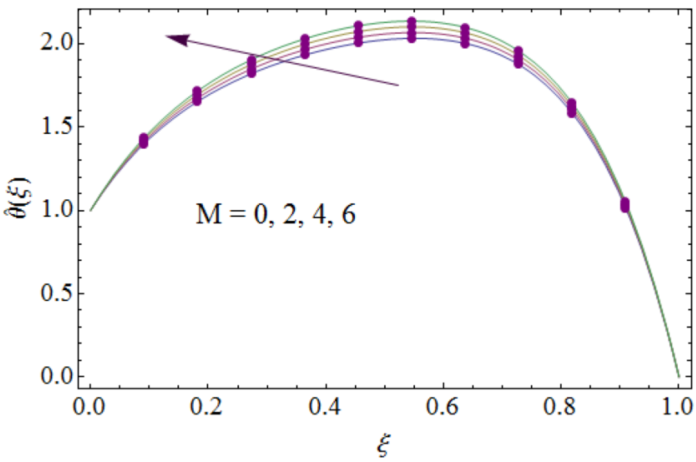

Fig. 15. $\widehat{\theta}(\xi)$ against M.

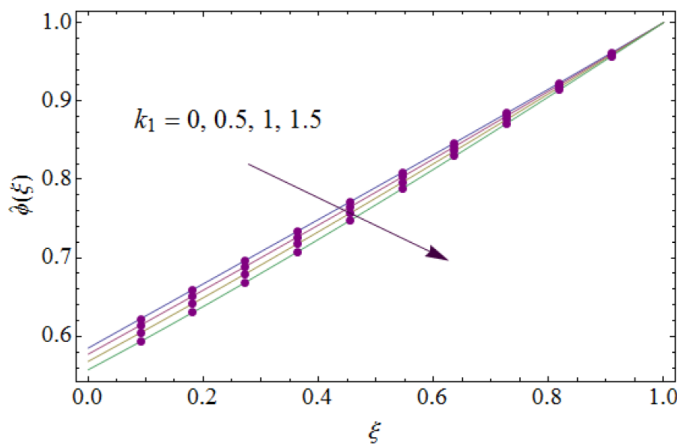

Fig. 16. $\widehat{\phi}(\xi)$ against k_1.

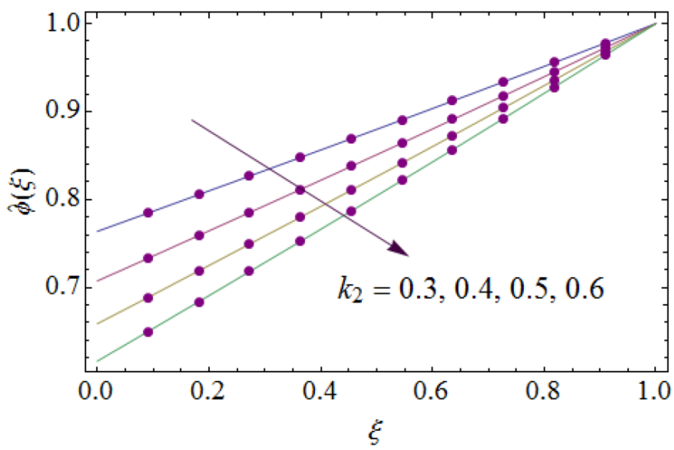

Fig. 17. $\widehat{\phi}(\xi)$ against k_2.

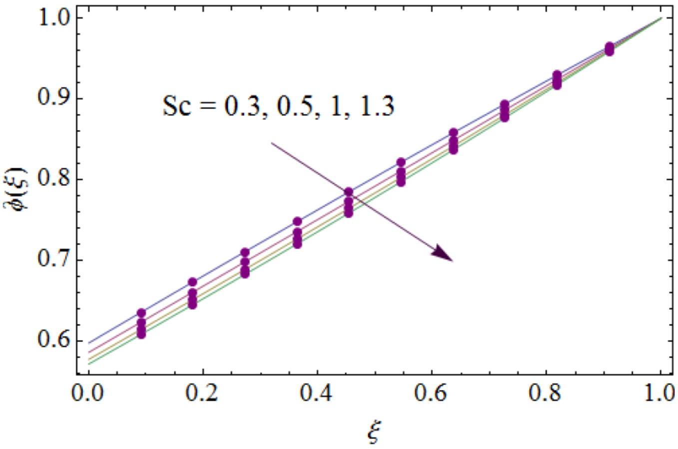

Fig. 18. $\widehat{\phi}(\xi)$ against Sc.

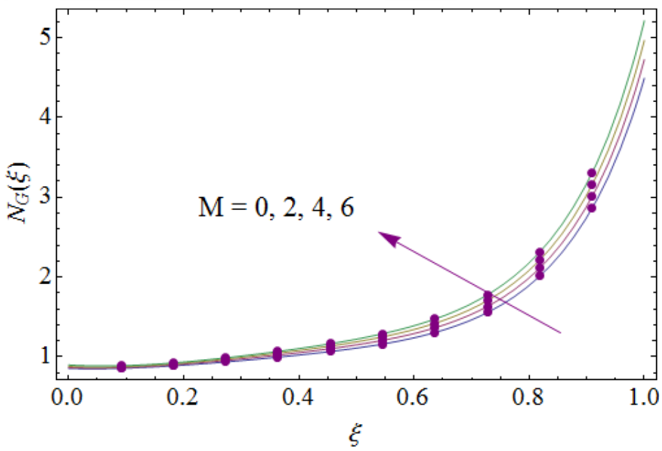

Fig. 19. $N_G(\xi)$ against M.

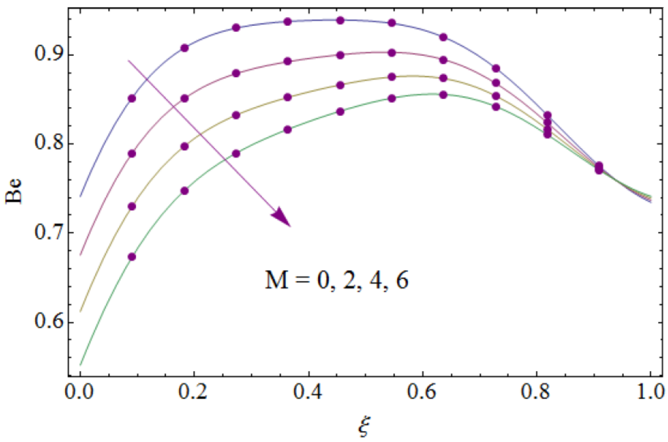

Fig. 20. Be against M.

7.4 Entropy rate

The impacts of Be and $(N_G(\xi))$ against magnetic parameter (M), ratio parameters (A_1, A_2), radiation parameter (R), Eckert number (Ec), homogeneous reaction variable (k_1), heterogeneous reaction variable (k_2), Brinkman number (Br), diffusion variable with respect to homogeneous reaction (L_1) and diffusion variable with respect to heterogeneous reaction (L_2) are sketched in figs. 19–38. Figures 19 and 20 depict the role of (M) on (Be) and $(N_G(\xi))$. From these figures, it is easily examined that $(N_G(\xi))$ increases *versus* $(M = 0.0, 2.0, 4.0, 6.0)$. Physically for higher (M) the

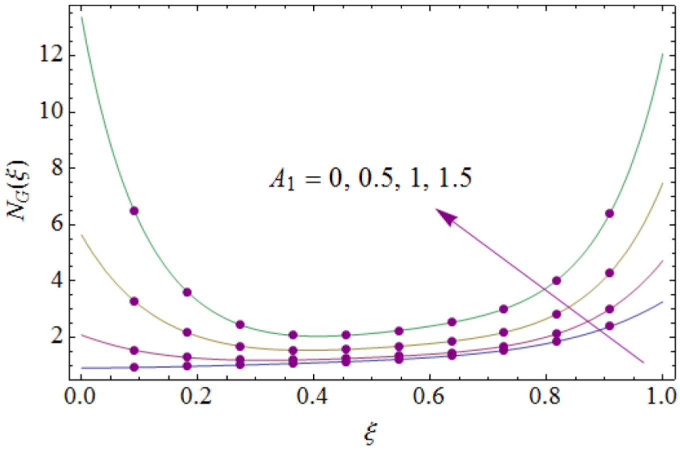

Fig. 21. $N_G(\xi)$ against A_1.

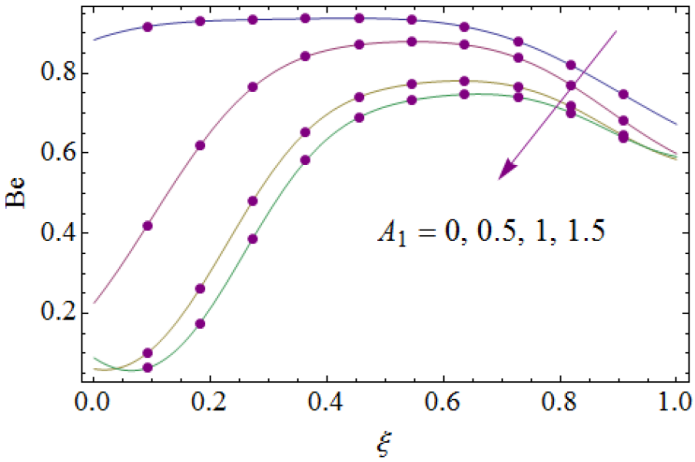

Fig. 22. Be against A_1.

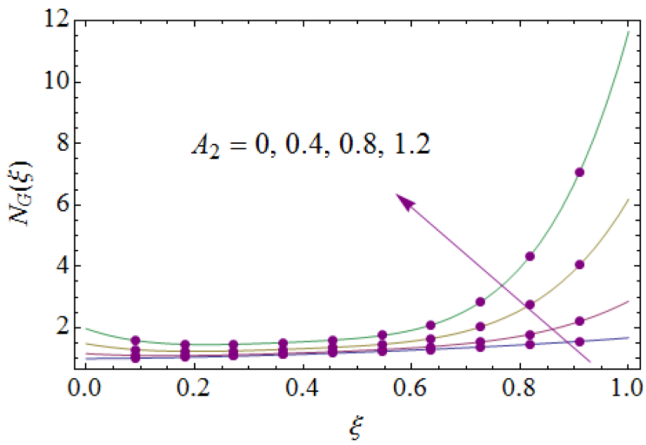

Fig. 23. $N_G(\xi)$ against A_2.

Lorentz force enhances which opposes the particles of liquid and therefore disorderedness increases. However, the opposite trend is examined for (Be) *versus* (M) (see fig. 20). Figures 21–24 are plotted to examine the behavior of variables ($A_1 = 0.0, 0.5, 1.0, 1.5$ and $A_2 = 0.0, 0.4, 0.8, 1.2$) on (Be) and $(N_G(\xi))$. Here the opposite trend is examined for (Be) and $(N_G(\xi))$ *versus* higher (A_1, A_2). Physically through larger (A_1, A_2), the stretching rates enhance which creates more disturbance in liquid particles and consequently boosts the disorderedness in the system. That is why

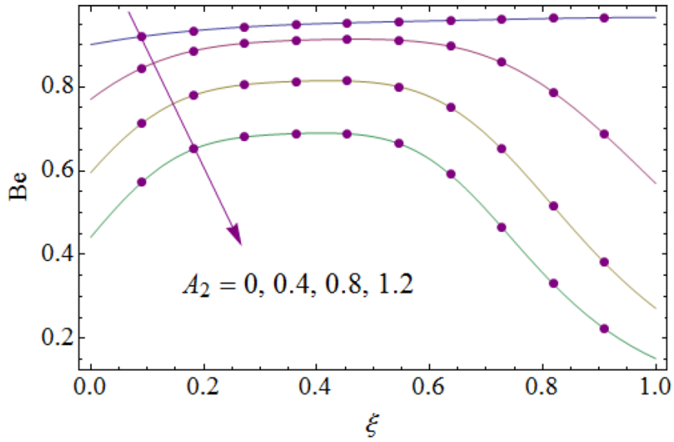

Fig. 24. Be against A_2.

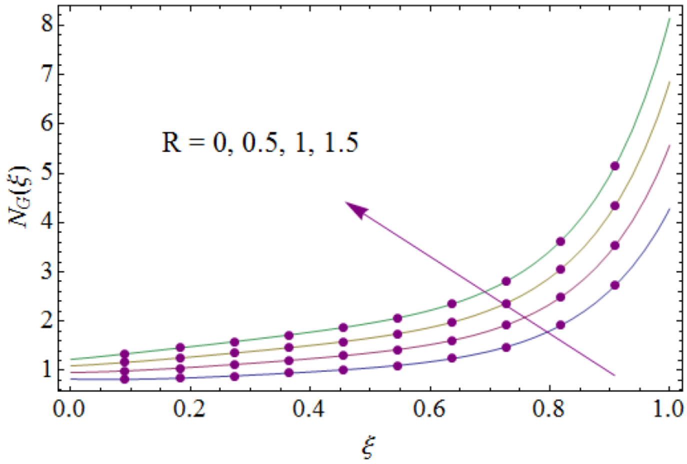

Fig. 25. $N_G(\xi)$ against R.

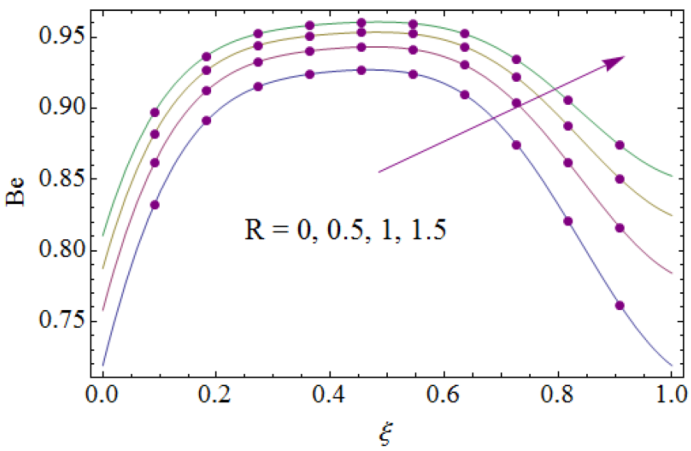

Fig. 26. Be against R.

$(N_G(\xi))$ is enhanced (see figs. 21 and 23). But opposite behavior for (Be) is presented in figs. 22 and 24. The variations in (Be) and $(N_G(\xi))$ due to the influence of radiation are sketched in figs. 25 and 26. Here both (Be) and $(N_G(\xi))$ monotonically increase via radiation ($R = 0.0, 0.5, 1.0, 1.5$). Physically more heat is produced in the presence of radiation in the system and as a result disorderedness increases. Therefore, both (Be) and $(N_G(\xi))$ are increased. Figures 27 and 28 are displayed for the effect of the Eckert number on (Be) and $(N_G(\xi))$. As we strengthen the (Ec), the (Be) and $(N_G(\xi))$ monotonically decrease close to the lower disk while these gradually boost near the upper disk when (Ec) attends the maximum range. Figures 29–32 analyze the behavior of ($k_1 = 0.0, 2.0, 4.0, 6.0$) and

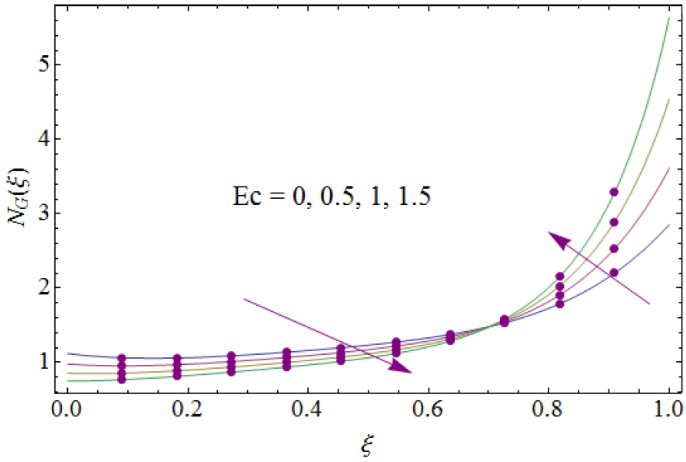

Fig. 27. $N_G(\xi)$ against Ec.

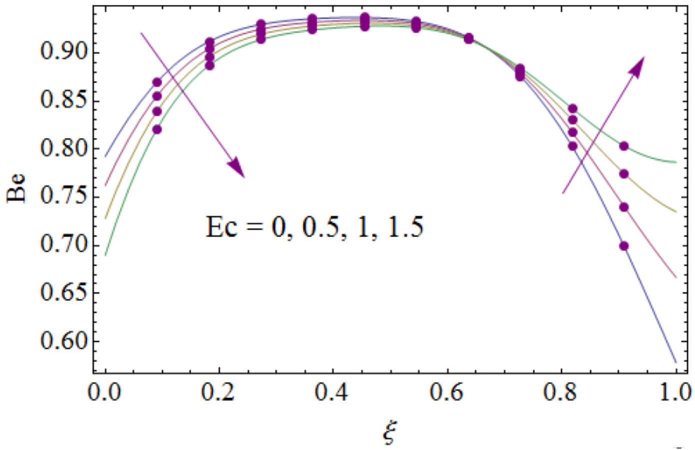

Fig. 28. Be against Ec.

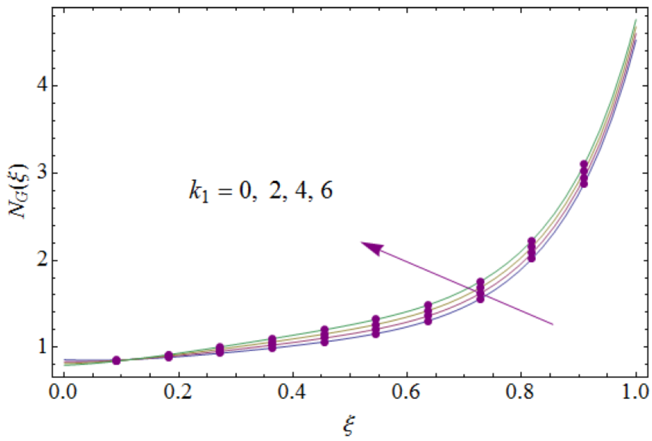

Fig. 29. $N_G(\xi)$ against k_1.

($k_2 = 0.0, 0.3, 0.6, 0.9$) on (Be) and ($N_G(\xi)$). Here both (Be) and ($N_G(\xi)$) monotonically boost *versus* homogeneous reaction and heterogeneous reaction parameters. Figures 33 and 34 are displayed to discuss how (Be) and ($N_G(\xi)$) vary via larger ($Br = 0.0, 0.4, 0.8, 1.2$). Here ($N_G(\xi)$) is increased for larger (Br). Physically for a larger Brinkman number the dissipation phenomenon generates less conduction rate which consequently boosts ($N_G(\xi)$). In fig. 34 it is noticed that when $Br = 0$ then $Be = 1.0$. Physically it means that for ($Br = 0$), the irreversibility disappears for

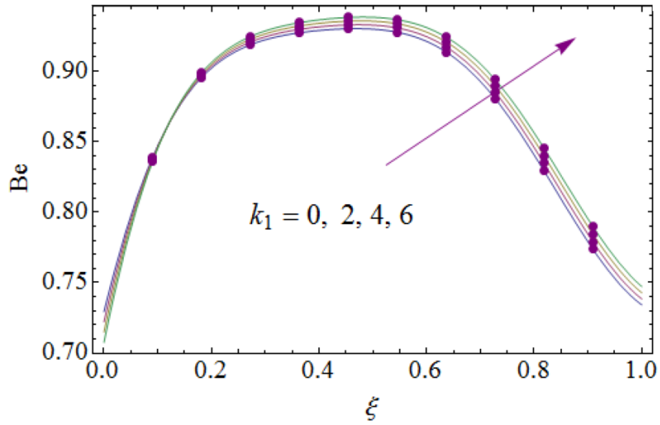

Fig. 30. Be against k_1.

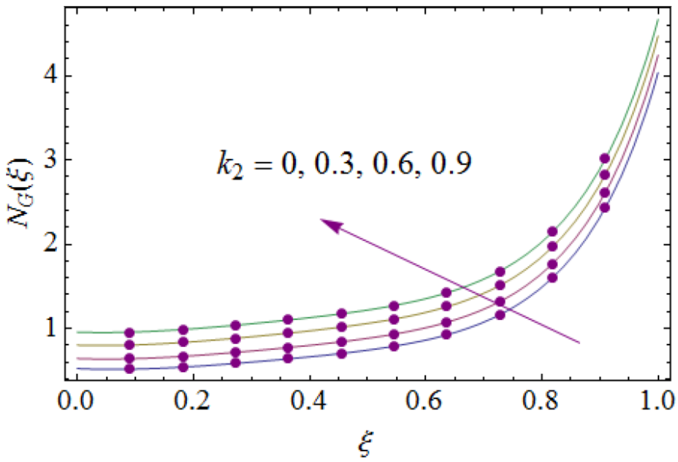

Fig. 31. $N_G(\xi)$ against k_2.

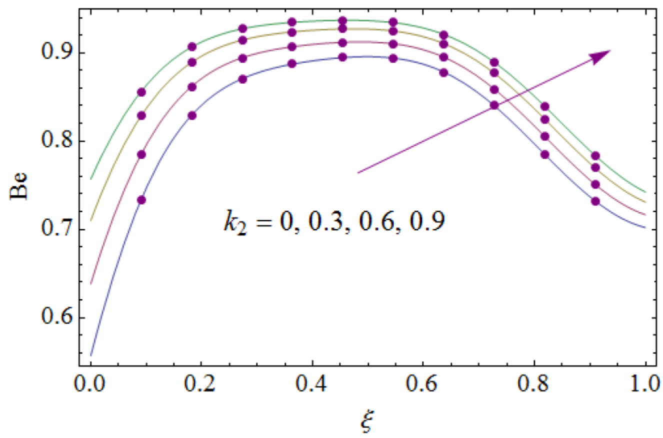

Fig. 32. Be against k_2.

viscous dissipation and only irreversibility associated with heat transfer is retained. There Be is maximum ($Br = 0.0$). When we enhance the estimation of the Brinkman number then Be gradually decreases. Figures 35–38 are plotted to analyze the salient aspects of (L_1) and (L_2) on (Be) and ($N_G(\xi)$). Here both (Be) and ($N_G(\xi)$) *versus* (L_1) decrease (see figs. 35 and 36). An opposite trend is noticed in the presence of (L_2) on (Be) and ($N_G(\xi)$) (see figs. 37 and 38).

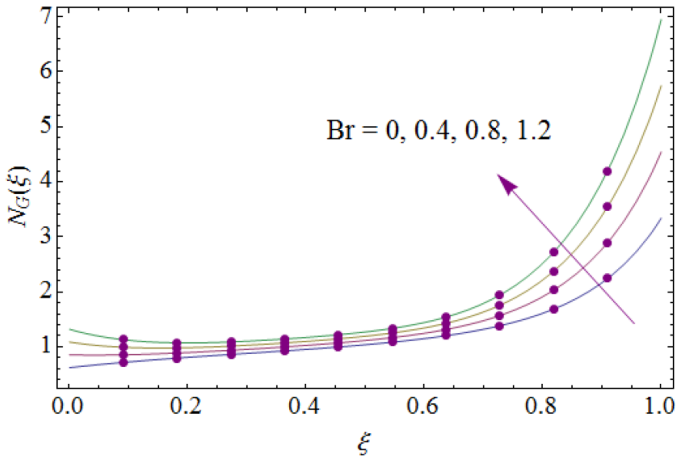

Fig. 33. $N_G(\xi)$ against Br.

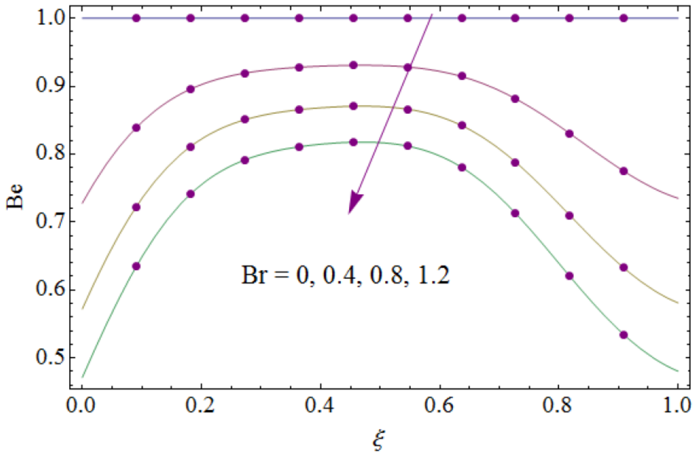

Fig. 34. Be against Br.

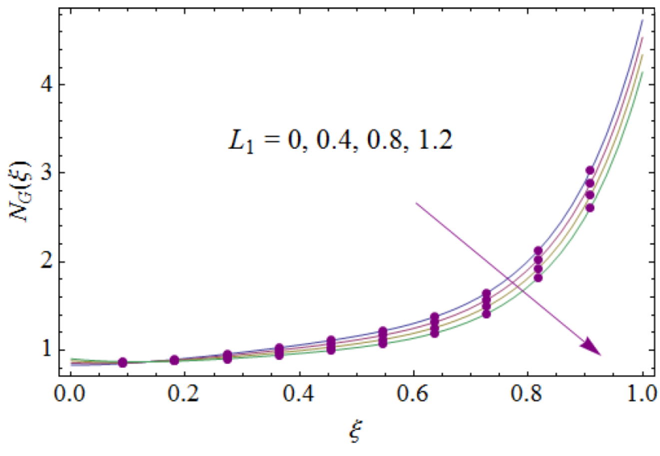

Fig. 35. $N_G(\xi)$ against L_1.

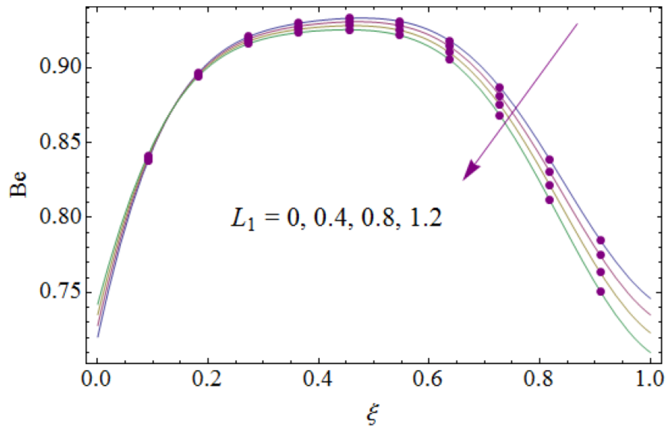

Fig. 36. Be against L_1.

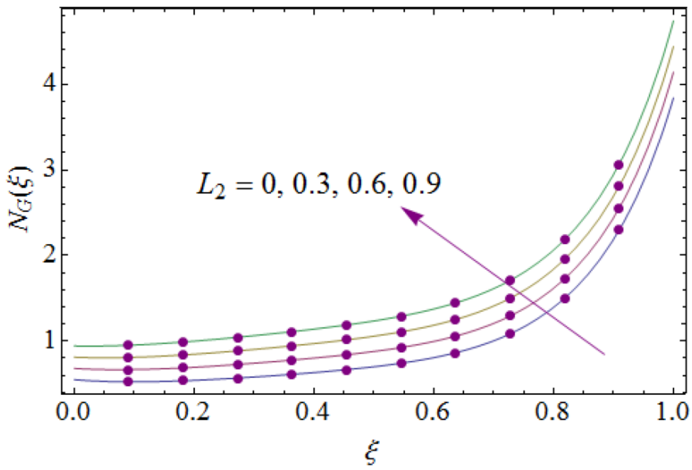

Fig. 37. $N_G(\xi)$ against L_2.

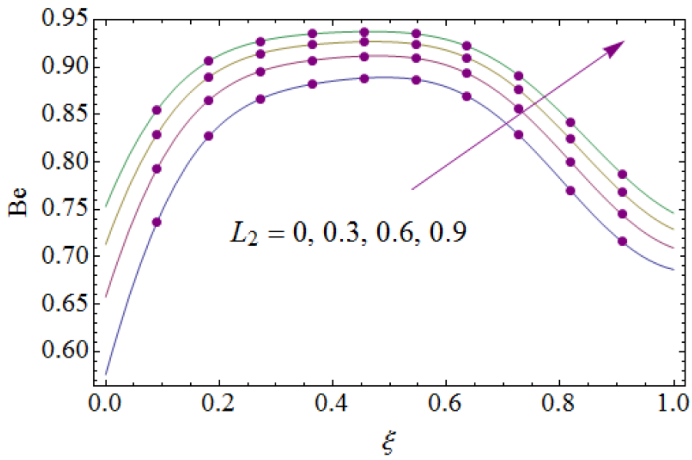

Fig. 38. Be against L_2.

8 Concluding remarks

Here irreversibility in radiative flow of viscous material between two rotating disks via quartic autocatalysis chemical reaction is addressed. The main outcomes of the present work are listed below:

- Magnitude of axial velocity decreases *versus* larger (Re).
- Tangential velocity is decreased by the magnetic parameter.
- Temperature decreases *versus* Prandtl number.
- For larger (k_1) and (k_2), concentration decreases.
- (Be) and ($N_G(\xi)$) show opposite trends for the magnetic variable.
- A dual trend is noticed for both (Be) and ($N_G(\xi)$) via Eckert number.

Nomenclature

u, v, w	velocity components	μ	dynamic viscosity
r, θ, z	Cartesian coordinates	σ°	Stefan Boltzmann constant
ρ	density	ε	constant pressure
$\tilde{p}$	pressure	Re	Reynolds number
ν	kinematic viscosity	M	magnetic parameter
σ	electrical conductivity	A_1, A_2	ratio parameter
B_0	magnetic field	Pr	Prandtl number
a_1, a_2	stretching rates of lower and upper disks	R	radiation parameter
h	distance between two disks	Ec	Eckert number
Ω_1, Ω_2	rotational velocities of lower and upper disks	A	dimensionless parameter
$\tilde{T}_1$	temperature at lower disk	Sc	Schmidt number
$\tilde{T}_2$	temperature at upper disk	k_1	homogeneous reaction parameter
ξ	space variable	k_2	heterogeneous reaction parameter
k°	mean absorption coefficient	δ	diffusion ratio
k	thermal conductivity	C_{f1}	skin friction at lower disk
τ_{zr}	shear stress in radial direction	C_{f2}	skin friction at upper disk
$\tau_{z\theta}$	shear stress in tangential direction	τ_w	total shear stress
Nu_{x1}	Nusselt number at lower disk	Nu_{x2}	Nusselt number at upper disk
R_r	local Reynolds number	L_2	diffusion variable with respect to heterogeneous reaction
Br	Brinkman number		
α_1	temperature difference parameter	L_1	diffusion variable with respect to homogeneous reaction
ρc_p	heat capacitance		
D_{C_1}, D_{C_2}	diffusion species coefficients	N_G	entropy generation rate
$\hat{C}_1$, $\hat{C}_2$	concentrations	c_p	specific heat capacity
		k_c, k_s	reaction rates

Publisher's Note The EPJ Publishers remain neutral with regard to jurisdictional claims in published maps and institutional affiliations.

References

1. T.V. Kármán, J. Appl. Math. Mech. **1**, 233 (1921).
2. T. Hayat, S. Qayyum, M.I. Khan, A. Alsaedi, Phys. Fluids **30**, 017101 (2018).
3. T. Hayat, M.I. Khan, A. Alsaedi, M.I. Khan, Int. Commun. Heat Mass Transfer **89**, 190 (2017).
4. M. Mustafa, Int. J. Heat Mass Transfer **108**, 1910 (2017).
5. W. Wu, B. Xiao, Ji. Hu, S. Yuan, Chenhui Hu, Appl. Therm. Eng. **133**, 33 (2018).
6. M. Hassan, C. Fetecau, A. Majeed, A. Zeeshan, J. Magn. & Magn. Mater. **465**, 531 (2018).
7. A. Mehmood, A. Zameer, M.A.Z. Raja, Appl. Soft Comput. **67**, 8 (2018).
8. S. Qayyum, M.I. Khan, T. Hayat, A. Alsaedi, Physica B **534**, 173 (2018).
9. S. Xun, J. Zhao, L. Zheng, X. Chen, X. Zhang, Int. J. Heat Mass Transfer **103**, 1214 (2016).
10. Y.Y. Lok, J.H. Merkin, I. Pop, Eur. J. Mech.-B/Fluids **72**, 275 (2018).
11. M.I. Khan, T. Hayat, A. Alsaedi, S. Qayyum, M. Tamoor, Int. J. Heat Mass Transfer **127**, 829 (2018).
12. S. Qayyum, M.I. Khan, T. Hayat, A. Alsaedi, M. Tamoor, Int. J. Heat Mass Transfer **127**, 933 (2018).
13. M.I. Khan, T. Hayat, M. Waqas, M.I. Khan, A. Alsaedi, J. Mol. Liq. **256**, 108 (2018).
14. S. Qayyum, T. Hayat, M.I. Khan, M.I. Khan, A. Alsaedi, J. Mol. Liq. **262**, 261 (2018).
15. T. Hayat, T. Nasir, M.I. Khan, A. Alsaedi, Results Phys. **9**, 390 (2018).
16. M.I. Khan, T. Hayat, A. Alsaedi, Phys. Fluids **30**, 023601 (2018).
17. Y. Liu, Y. Jian, W. Tan, Int. J. Heat Mass Transfer **127**, 901 (2018).
18. M.I. Khan, T. Hayat, S. Qayyum, M.I. Khan, A. Alsaedi, Phys. Lett. A **382**, 2343 (2018).
19. E. Manay, E.F. Akyürek, B. Sahin, Results Phys. **9**, 615 (2018).
20. X. Tian, L. Wang, Int. J. Heat Mass Transfer **121**, 1137 (2018).
21. Z. Li, M. Sheikholeslami, M. Jafaryar, A. Shafee, A.J. Chamkha, J. Mol. Liq. **266**, 797 (2018).
22. G.H.R. Kefayati, H. Tang, Int. J. Heat Mass Transfer **120**, 683 (2018).
23. M.I. Khan, S. Qayyum, T. Hayat, M.I. Khan, A. Alsaedi, T.A. Khan, Phys. Lett. A **382**, 2017 (2018).
24. T. Hayat, S. Nawaz, A. Alsaedi, J. Mol. Liq. **248**, 447 (2017).
25. Z.Y. Xie, Y.J. Jian, Energy **139**, 1080 (2017).
26. T. Hayat, M.W.A. Khan, M.I. Khan, A. Alsaedi, J. Braz. Soc. Mech. Sci. Eng. **40**, 373 (2018).
27. M.I. Khan, S. Qayyum, T. Hayat, A. Alsaedi, Chin. J. Phys. **56**, 1525 (2018).
28. S. Ahmad, M.I. Khan, T. Hayat, M.I. Khan, A. Alsaedi, Colloids Surf. A **554**, 197 (2018).
29. T. Hayat, F. Shah, M.I. Khan, M.I. Khan, A. Alsaedi, J. Mol. Liq. **266**, 814 (2018).
30. T. Hayat, M.I. Khan, T.A. Khan, M.I. Khan, S. Ahmad, A. Alsaedi, J. Mol. Liq. **265**, 629 (2018).
31. S.J. Liao, *Homotopy Analysis Method in Non-linear Differential Equations* (Springer and Higher Education Press, Heidelberg, 2012).
32. T. Hayat, M.I. Khan, S. Qayyum, M.I. Khan, A. Alsaedi, J. Mol. Liq. **264**, 375 (2018).
33. A. Jafarimoghaddam, H. Aberoumand, S. Aberoumand, A.A.A. Arani, A. Habibollahzade, Eng. Sci. Technol. **20**, 1515 (2017).
34. T. Hayat, F. Haider, T. Muhammad, A. Alsaedi, J. Mol. Liq. **233**, 278 (2017).
35. T. Hayat, M. Rashid, M.I. Khan, A. Alsaedi, Results Phys. **9**, 1618 (2018).
36. T. Hayat, M.I. Khan, M. Farooq, A. Alsaedi, M. Waqas, T. Yasmeen, Int. J. Heat Mass Transfer **99**, 702 (2016).
37. M.I. Khan, M. Waqas, T. Hayat, A. Alsaedi, J. Colloid Interface Sci. **498**, 85 (2017).
38. T. Hayat, M.I. Khan, M. Farooq, T. Yasmeen, A. Alsaedi, J. Mol. Liq. **220**, 49 (2016).
39. T. Hayat, M.I. Khan, S. Qayyum, A. Alsaedi, Colloids Surf. A **539**, 335 (2018).
40. M.I. Khan, T. Hayat, M.I. Khan, A. Alsaedi, Int. Commun. Heat Mass Transfer **91**, 216 (2018).
41. M.I. Khan, T. Hayat, A. Alsaedi, Results Phys. **7**, 2644 (2017).
42. M.I. khan, S. Ullah, T. Hayat, M.I. Khan, A. Alsaedi, J. Mol. Liq. **260**, 279 (2017).
43. T. Hayat, S. Ahmad, M.I. Khan, A. Alsaedi, Physica B **537**, 116 (2018).
44. A. Alsaedi, M.I. Khan, T. Hayat, J. Theor. Comput. Chem. **16**, 1750064 (2017).
45. T. Hayat, F. Shah, M.I. Khan, A. Alsaedi, T. Yasmeen, Micrograv. Sci. Technol. **29**, 459 (2017).